Contents lists available at ScienceDirect



# Journal of Magnetic Resonance

journal homepage: www.elsevier.com/locate/jmr



# Diamond rotors for high magic angle spinning frequencies

Lauren Schaffer <sup>a,1</sup>, David Preiss <sup>b,2</sup>, Ravi Shankar Palani <sup>a</sup>, Nicholas Wiesner <sup>a</sup>, Jiaming Liu <sup>b</sup>, Samuel Strymish <sup>a</sup>, Salima Bahri <sup>a,3</sup>, Sara Linse <sup>c</sup>, Neil Gershenfeld <sup>b,\*</sup>, Robert G. Griffin <sup>a,\*</sup>

- a Department of Chemistry and Francis Bitter Magnet Laboratory, Massachusetts Institute of Technology, Cambridge, MA 02139, United States
- <sup>b</sup> Center for Bits and Atoms, Massachusetts Institute of Technology, Cambridge, MA 02139, United States
- <sup>c</sup> Department of Biochemistry and Structural Biology, University of Lund, Sweden

#### ABSTRACT

Magic Angle Spinning (MAS) nuclear magnetic resonance (NMR) spectroscopy is limited in spectral resolution by the spinning frequency of rotors that hold the analyte. Traditional yttria-stabilized zirconia (YSZ) rotors have mechanical constraints that typically limit spinning frequencies of 0.7 mm rotors to  $\omega_r/2\pi \sim 110$  kHz. These frequencies are not sufficient to achieve resolution comparable to that of solution NMR, which theoretically requires  $\omega_r/2\pi > 300$  kHz. Building upon prior work that utilized rotary-assisted drilling, we present significant advances in diamond rotor fabrication using a high precision lathe and a centerless laser machining fixture that achieves improved concentricity of the rotor outer and inner diameters and spinning stability. The new crop of diamond rotors, which interface with the Bruker MAS 3 spinning system equivalently or better than commercial rotors, spun using automatic 0.7 mm profiles. Furthermore, diamond rotors can be emptied and repacked, and we describe a set of 3D-printed centrifuge tools for efficient execution of this process. We evaluate chemical vapor deposition (CVD) versus high-pressure high-temperature (HPHT) diamonds as rotor material and find HPHT preferable. Extended spin stability tests and multidimensional NMR spectra of  $A\beta_{1-40}$  demonstrate the robustness and usability of these rotors. These advances pave the way for higher frequency spinning with helium gas in the future, enabling transformative improvements in MAS NMR for biological and material sciences.

### 1. Introduction

Magic angle spinning (MAS) nuclear magnetic resonance (NMR) spectroscopy has evolved as an indispensable tool for investigating molecular structures and dynamics in crystalline, non-crystalline and insoluble biological systems [1]. Its capability to resolve atomic-level details in complex systems has catalyzed breakthroughs in structural biology, particularly in the study of amyloid fibrils [2–12], membrane proteins [13–16], and macromolecular assemblies [17–20]. Its application stretches to the field of material sciences, being vital, but not limited, to the study of battery and other energy research materials [21,22]. Despite these successes, the utility of MAS NMR remains constrained by the spinning frequency of the MAS rotors, which directly impacts spectral resolution and sensitivity [23,24].

Traditional MAS rotor materials, such as yttria-stabilized zirconia (YSZ) and sapphire, have dominated the field due to their availability and mechanical properties [25]. However, the inherent material strength of YSZ sets an upper limit on achievable spinning frequencies,  $\omega_r/2\pi$ , which for 0.7 mm rotors is *typically*  $\sim 110$  kHz when using N<sub>2</sub> or

air as the driving fluid. We note that values of  $\omega_r/2\pi\sim 120$  kHz for 0.7-and 0.75-mm rotors  $ZrO_2$  have been reported and we achieved  $\omega_r/2\pi=125$  kHz using a diamond rotor. While these spinning frequencies enable  $^1H$  detected MAS experiments and provide valuable insights into biomolecular systems, they fall short of the theoretical requirements,  $\omega_r/2\pi>300$  kHz, for achieving solution-like linewidths and coherence lifetimes in solid-state NMR [23,26]. In addition, sensitivity enhancements in dynamic nuclear polarization (DNP) NMR are directly proportional to the microwave power incident upon the sample, after passing through the rotor material. YSZ has a suboptimal transmission coefficient at the microwave frequencies (currently 250  $\rightarrow$  593 GHz) relevant for high-field DNP NMR [27]. While sapphire is more transparent to microwaves and has better thermal conductivity than YSZ, it is a fragile material that has not been used at the highest spinning frequencies.

To address these limitations, diamond has emerged as a promising material for fabrication of MAS rotors. The exceptional mechanical properties of single-crystal, high-pressure high-temperature (HPHT) diamond, including its high fracture toughness, low density, and exceptional thermal conductivity, position it as a superior alternative to

 $<sup>^{\</sup>ast} \ \ Corresponding \ authors.$ 

E-mail addresses: gersh@cba.mit.edu (N. Gershenfeld), rgg@mit.edu (R.G. Griffin).

<sup>&</sup>lt;sup>1</sup> Present address: Department of Chemistry, Columbia University, New York, New York

 $<sup>^{2}\,</sup>$  Present address: Variable Machines, 303 Broadway, Cambridge, MA 02139

<sup>&</sup>lt;sup>3</sup> Present address: Department of Chemistry, Utrecht University, The Netherlands

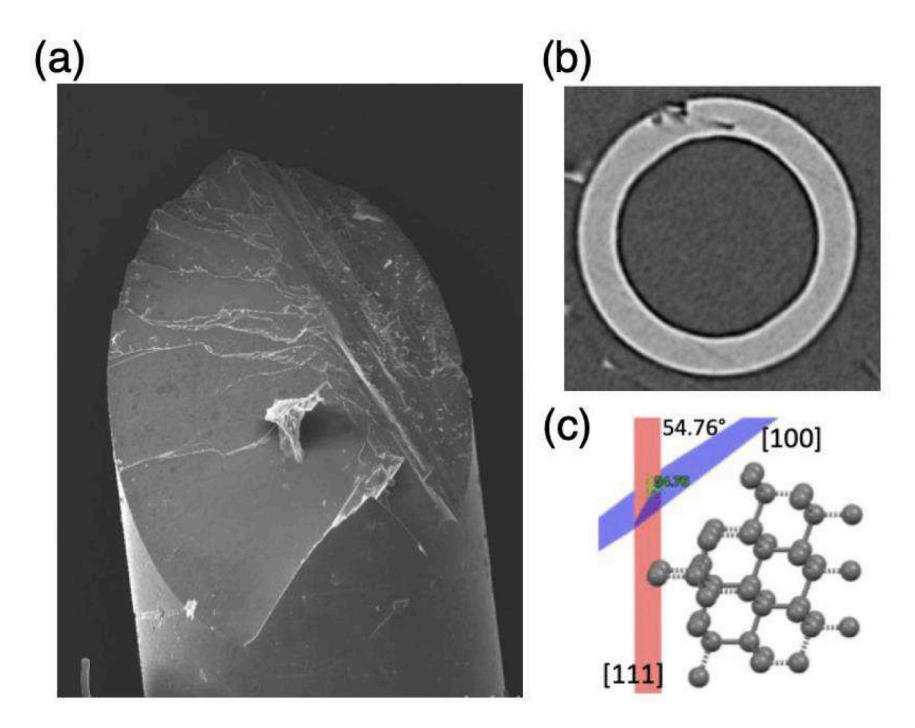


Fig. 1. This figure illustrates the challenges associated with machining diamond. (a) A SEM image shows cleavage along the [111] plane, attributed to intrinsic crystallographic weaknesses and thermal mismatch stresses, resulting in flat cleavage surfaces. (b) A micro-Computed Tomography (CT) cross-section reveals the internal extent of the chipping in a CVD diamond sample. (c) A crystallographic representation using Mercury software shows the [111] cleavage plane relative to the [100] machining orientation, illustrating the 54.76° angle between these planes in the diamond lattice.

zirconia [27,29]. These properties make it an ideal candidate for achieving higher spinning frequencies with helium gas, which at room temperature has a speed of sound, which determines the maximum spinning frequency of a rotor, that is about x3 higher than N<sub>2</sub>. Furthermore, diamond's high transparency to terahertz radiation enhances microwave transmission, a critical parameter for improving DNP efficiency. In addition, recent work from our group demonstrated the paramagnetic P1 centers present in high-pressure high-temperature (HPHT) diamond itself can serve as polarizing agents that produce <sup>13</sup>C DNP enhancement factors of  $\sim$ 500 [30]. Although significant challenges remain in efficiently extracting polarization from the diamond lattice, these intrinsic properties of P1 diamond could potentially eliminate the need for externally added polarizing agents in DNP experiments conducted in diamond rotors. Finally, the exceptional thermal conductivity of diamond enables the sample to be efficiently cooled, circumventing the aerodynamic heating associated with high frequency spinning. Despite these well-known advantages, the high strength and hardness of diamond have precluded its use in MAS experiments due to machining challenges in rotor fabrication.

Recent advances in laser micromachining described here have overcome these barriers, enabling the fabrication of diamond MAS rotors with low tolerances and aspect ratios of  $\sim$ 9. The first generation of diamond rotors, fabricated using rotary-assisted drilling described in our prior work [27,29], demonstrated the feasibility of machining 0.7 mm diamond rotors that achieve stable spinning at 111 kHz. While these initial successes represent a crucial step toward leveraging diamond's material advantages to enhance MAS NMR performance, they did not produce rotors with the required inner/outer diameter concentricity or with the desired inner and outer diameter tolerances. This manuscript describes major advances in diamond rotor fabrication that address these issues. First, using a custom designed high precision lathe for machining the outer diameter of the rotors, we now achieve a axial tolerance under 2 µm. Second, to machine the high aspect ratio inner diameter, we have designed and assembled a centerless machining apparatus that replaces the rotary-assisted drilling described in our prior work. The centerless fixture greatly improves control of the size of the inner diameter and the concentricity with the outer diameter. Third, the diamond rotors are mechanically robust, and we have repeatedly packed and unpacked the rotors we have fabricated. This process is facilitated by the development of new set of 3D-printed centrifuge tools. Fourth, we evaluate alternative diamond sources, comparing the performance of chemical vapor deposition (CVD) and high-pressure high-temperature (HPHT) diamonds in rotor fabrication. Fifth, we also report extended-duration spin stability tests for these rotors highlighting their robustness. In addition, we report 3D  $^1\mathrm{H-}$  and  $^{13}\mathrm{C-}$  detected NMR spectra of the Alzheimer's protein A $\beta_{1-40}$ , obtained with these new rotors, demonstrating their usability in cutting-edge MAS NMR applications.

By addressing the limitations of current MAS rotor technology, with a potential to spin at higher frequencies than with YSZ rotors using helium gas, our work contributes to advancing solid-state NMR spectroscopy. The introduction of diamond rotors offers significant opportunities for improving both resolution and sensitivity in studies of complex biological systems and materials.

## 2. Methods

# 2.1. Rotor fabrication

The fabrication of diamond rotors capable of achieving ultra-high spinning frequencies requires overcoming significant machining challenges due to diamond's exceptional hardness. Building upon previous work utilizing rotary-assisted drilling, we have developed an advanced fabrication protocol employing laser micromachining with custom-designed mechanical fixtures to achieve the necessary precision and concentricity for stable high-speed MAS. This protocol involves two primary stages: machining the outer diameter (OD) using a high-precision air bearing lathe, followed by machining the inner diameter (ID) with a novel centerless apparatus.

Rotors were fabricated with an Oxford Lasers (Didcot, Oxfordshire, UK) A-series laser micromachining system equipped with a Q-switched

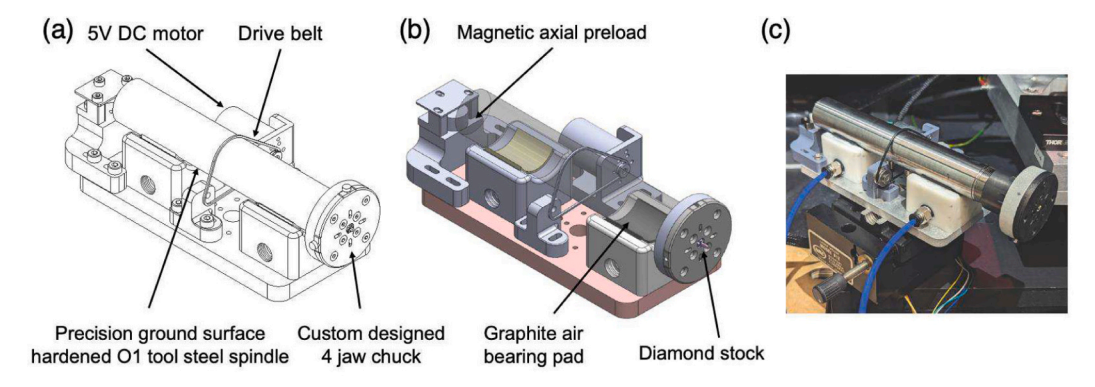


Fig. 2. Custom-built high-precision air bearing lathe used for machining the OD of the diamond rotors. (a) A wire frame diagram showing the overall assembly, highlighting the DC drive motor, drive belt, precision ground spindle, and the custom 4-jaw chuck. (b) A sectional 3D CAD view reveals internal components, including the graphite air bearing pads that provide low-friction, high-precision rotation, the magnetic axial preload mechanism, and the positioning of the diamond stock within the chuck. (c) A photograph shows the physical assembled lathe.

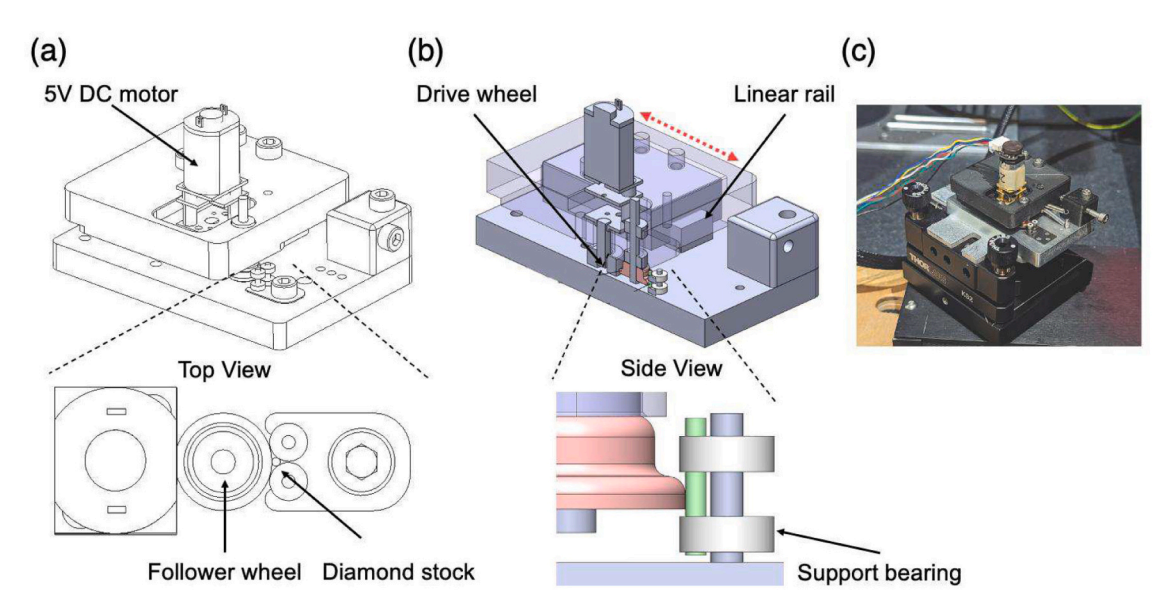


Fig. 3. The centerless machining fixture for fabricating the inner diameter (ID) of the diamond rotors. (a) A wire frame model plus detailed top view, showing the driving mechanism and a close-up schematic depicting the diamond stock positioned between the drive wheel and follower wheels. (b) An isometric cross sectional CAD view shows the side perspective, indicating the drive wheel mounted on a linear rail for controlled engagement and the support bearings that guide the diamond rotor. (c) A photograph displays the assembled centerless fixture integrated onto its positioning stage. This design ensures high concentricity between the ID and OD by eliminating external clamping fixtures.

532 nm diode-pumped Nd:YAG laser with a spot size of 15 µm. The pulse duration was 20 ns at a repetition rate of 5 kHz. High pressure, high temperature (HPHT) single crystal diamond logs with dimensions of 1  $\times$ 1 × 6 mm were purchased from Dutch Diamond Company (Cuijk, Netherlands) and Element6 (Didcot, Oxfordshire, UK). Chemical vapor deposition (CVD) single crystal diamond logs of the same dimension were procured from Element6. The diamond was purchased and machined along the [100] orientation (Miller indices) to avoid the cleavage plane along the [111] direction as shown in Fig. 1 (C). The theoretical strength of diamond is highly dependent on crystal orientation and cleavage in the [111] plane is dominant [31]. Due to the intrinsic diamond/substrate thermal mismatch stresses in chemical vapor deposition diamond, CVD diamonds have higher dislocation density than that of HPHT diamond. Empirical evidence of the frequency of fractures during machining also proves that HPHT diamond generally fractures less than CVD diamond shown in Fig. 1(a) and (b). Thus, HPHT diamond is the better suited for diamond rotors.

The rotor OD (outer diameter) is machined using a custom-built high-precision lathe incorporating graphite air bearings to minimize vibration and ensure rotational accuracy shown in Fig. 2. This design contrasts with initial concepts using angular contact bearings [27,29], which presented challenges in cost, preloading, and alignment. The lathe incorporates features like adjustable radial preload via magnets and pitch/yaw adjustment for precise alignment of the rotary axis. The lathe is attached to the Aerotech stage inside the laser machining system through a Kelvin kinematic coupling. Key improvements during development included optimizing the axial constraint, moving from a potentially noisy bearing to an axial bushing or exploring planar air bearings, and implementing closed-loop speed control using a quadrature encoder and PID controller to maintain a constant speed setpoint and improve surface finish. Addressing issues like pneumatic hammer through precision regulators and optimizing machining parameters, such as feed rates and axial machining depth, were crucial for achieving consistent results. The diamonds are mounted in the precision ground O1 tool steel spindle through a custom made 4 jaw chuck, made with 3D printed 314 stainless steel body and titanium jaws machined on 5 axis waterjet machines finished with hand fitting and polishing. The outer diameter as well as taper and concentricity were measured with a

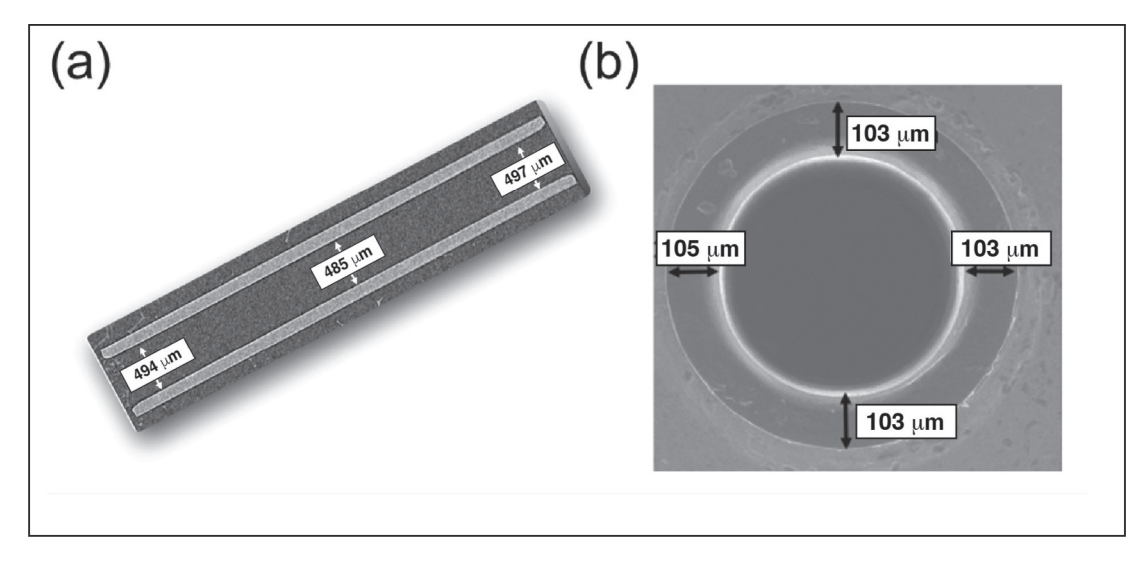
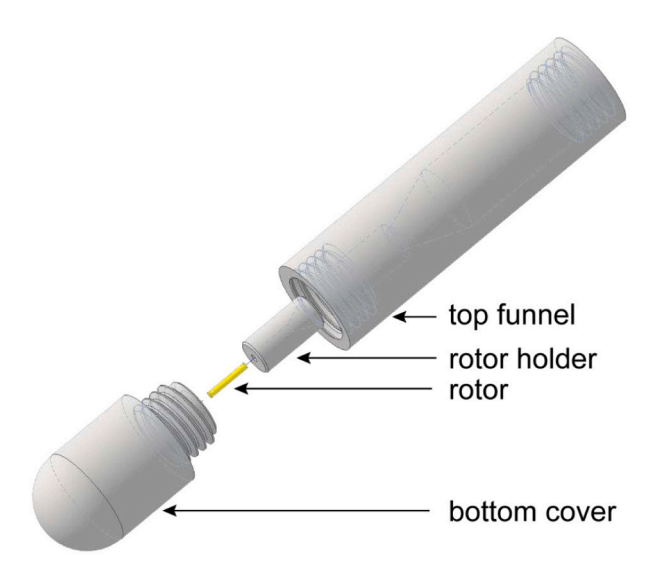


Fig. 4. Characterization of a completed diamond rotor fabricated using the described methods with dimensions for Rotor 2. (a) A micro-CT cross-sectional reconstruction provides a view of the entire rotor 4.6 mm rotor length, showing the uniformity of the inner bore with measured ID dimensions. Note that for Rotor 2 there is a  $\sim$ 2% narrowing of the ID in the center of the rotor, a residual taper. This was a feature observed in all the rotors. (b) An SEM image of a rotor end-face cross-section. The wall thickness measurements were performed by subtracting the ID from the OD and dividing by two. This avoided the necessity of aligning the rotor precisely for end on measurements.



**Fig. 5.** An exploded view of the 3D-printed rotor packing tool, illustrating its components: top funnel, rotor holder, rotor, and bottom cover. This tool is designed for packing biological samples into rotors using a swinging-bucket ultracentrifuge, ensuring efficient and compact pellet formation.

Keyence TM-X5000 Telecentric Non-contact Laser Measurement System throughout the machining process until the desired diameter of 700  $\mu m$  (± 3  $\mu m$ ) was achieved.

After reaching the desired rotor OD the rotor body was then parted off from the stock and scanned for chips and irregularities using a Rigaku CT Lab HX130 (Micro Computed-Tomography) scanner at 2.1- $\mu$ m voxel resolution. If the diamond round part was free from defects, then it will proceed to inner diameter machining.

Following OD machining, the high aspect ratio ID is fabricated using a custom-designed centerless machining apparatus show in Fig. 3. This fixture, inspired by centerless grinding principles, secures the diamond rotor between free-spinning bearings and a rotating drive mechanism (e. g., an O-ring or roller), eliminating the need for external centering fixtures. This approach intrinsically maximizes the concentricity between the ID and OD. The rotor body rests against guide bearings while being

rotated by the drive mechanism, which is mounted on a linear stage preloaded by a spring to ensure uniform contact force. The angle of the drive mechanism can be adjusted to control axial loading.

Laser machining of the ID involves multiple passes. Initial rough passes are performed with 100 % laser power and a 5 kHz repetition frequency, from both ends of the rotor to establish the basic bore and minimize taper. Subsequent finishing passes at 70 % laser power at 50 kHz frequency achieve the final target ID about 470-500 μm and uniform interior surface. Optimization of the toolpath strategy was essential; for instance, switching from bidirectional radial machining to unidirectional passes resolved issues with internal cracking or lobed fractures observed in CT scans. Throughout the development, various challenges were addressed, including material transfer from bearings, rotor 'walking' out of centerless fixture, cracking potentially linked to stock size/centering, thermal effects, machining strategy, or backscatter, and rotational pausing during laser machining. Solutions involved optimizing shim materials, drive mechanisms (material, geometry), rotational speed, drive preload, and improving stage alignment. Postmachining cleaning employed a aqua regia (nitro hydrochloric acid) bath to remove traces of metallic contaminants followed by hightemperature heat treatment to eliminate the graphite residue. The final dimensions and concentricity are verified using micro-CT, SEM, and gage pins.

Fig. 4 shows a cross-sectional view of a completed rotor and scans of rotor cross section showing the concentricity of the inner and outer diameters. The dimensions on the figure are from Rotor 2 and a complete compilation of the dimensions of each of the four rotors is provided in the Supporting information. We provide this detailed data since it shows the typical variations encountered with our current laser machining instrument and protocol. As might be expected the OD is easier to machine and the average for the four rotors is  $701.2 \, \mu m$ . The average ID of the ends is 491.6 µm and one end was always slightly larger than the other and was used to insert the drive tip since the stem was longer than in the bottom cap. To calculate the wall thickness, we subtracted the ID from the OD and divided by two. This avoided measurements of the wall thickness from the top and bottom which were difficult since the rotor needed to be carefully aligned vertically. Although the taper was largely suppressed by the machining protocol described above, a residue persisted and the average ID in the center of each rotor was narrower than at the ends. For the four rotors described here the average central ID was

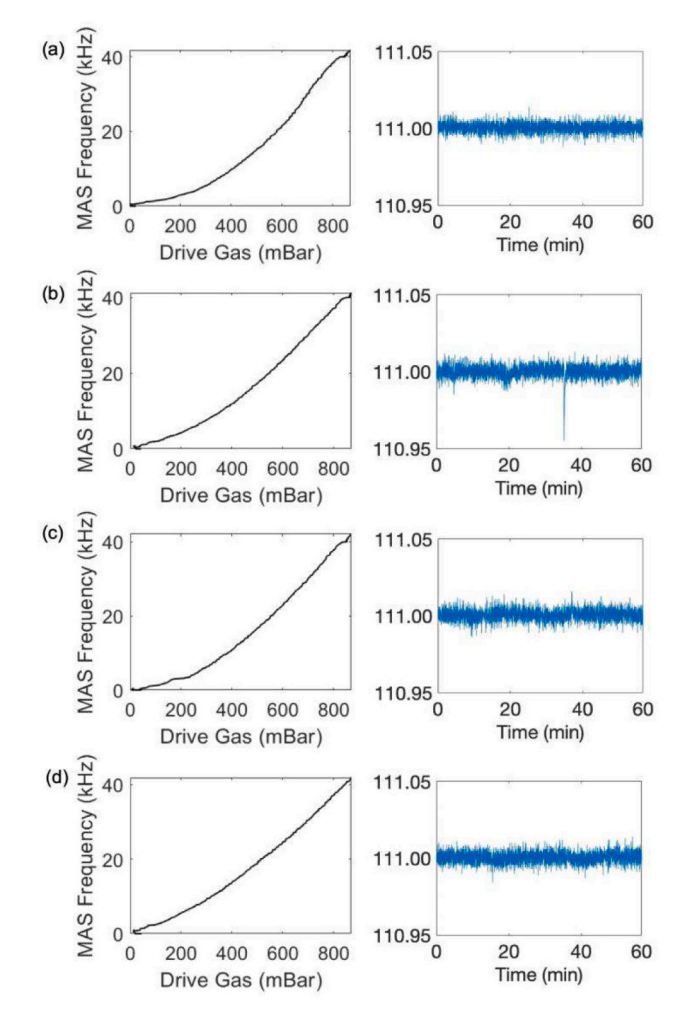


**Fig. 6.** A-D. Rotor spin up profiles and stability tests for diamond rotors 1–4, respectively. Rotors were spun using the Bruker automatic 0.7 mm profile, no added stabilizer (zirconia powder). MAS frequency profiles of 4 new diamond rotors spinning up from 0 to 40 kHz under constant bearing gas pressure are plotted in the left column. Rotor stability profiles, at 111 kHz for 1 h, are in the right column. Standard deviations across the spinning period are A) 3.29 Hz, B) 4.28 Hz, C) 3.83 Hz, and D) 3.72 Hz.

**Table 1** Drive pressures (in millibar) for 0.7 mm rotors, including a Bruker 0.7 mm ZrO $_2$ , previously reported diamond rotor version 1, and 4 newly machined diamond rotors (Rotors 1, 2, 3, and 4). All rotors at all MAS frequencies were spun on the MAS 3 using Bruker automatic mode with constant bearing pressure between 2500 and 2700 millibar.

Diamond						
MAS Freq. (kHz)	$\begin{array}{c} 0.7 \\ ZrO_2 \end{array}$	v.1	Rotor 1	Rotor 2	Rotor 3	Rotor 4
40	876	840	907	898	860	853
50	1018	987	1049	1033	990	987
60	1149	1176	1187	1190	1120	1109
70	1362	1489	1490	1462	1429	1402
80	1736	1842	1860	1647	1789	1780
90	2130	2249	2270	2016	2191	2202
100	2680	2707	2730	2678	2662	2684
110	3469	3273	3390	3338	3269	3313

475.7  $\mu m$  which was 15.9  $\mu m$  smaller, yielding a taper of 3 %.

This refined fabrication process yields diamond rotors with tolerances and concentricity ( $\sim$ 2  $\mu$ m) suitable for stable spinning at 111 kHz

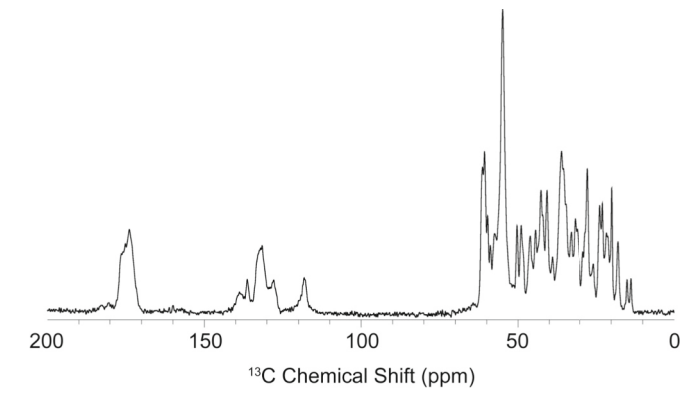


Fig. 7.  $^{13}$ C CPMAS spectrum of U— $^{13}$ C,  $^{15}$ N-A $\beta_{1-40}$  spinning at  $\omega_r/2\pi=100$  kHz in an HPHT diamond rotor.

using standard MAS systems, demonstrating performance comparable or superior to commercial zirconia rotors.

### 2.2. Rotor packing tools

A set of 3D printed 0.7 mm rotor centrifugal packing tools were developed for the purpose of packing samples which require hydration control and rapid transfer into rotors while maintaining sample integrity. These samples, such as amyloid fibrils and membrane proteins, are often isotopically labeled and successful handling is dependent on user dexterity. 3D printable centrifuge packing devices can ensure an efficient, dependable, and accessible way to pack valuable samples into very small rotors. While centrifuge packing tools have been regularly used for larger rotor sizes, especially 1.3 mm rotors, standard practice has been to pack 0.7 mm rotors nestled inside of a 1.3 mm rotor itself. Unlike other 3D printable packing tools, ours illustrated in Fig. 5 do not require additional parts such as O-rings, pipette tips, or expensive 1.3 mm rotors [32–34]. To avoid sample clogging at the funnel exit, the rotor is connected to the base of the funnel.

The design is simple in concept and execution. The tools consist of 3 parts: rotor holder, top funnel, and bottom cover. The top funnel and the bottom cover mate via 3D printed threads with the rotor holder compressed between the two. The pieces were printed with Durable V2 resin on a Formlabs Form 3 stereolithography (SLA) 3D-printer (Formlabs, Somerville, MA, US) with 50 µm layer thickness. The prints were oriented so the long axis of the packing tool is vertical in the printer such that the spacing of the threads is handled by the z-axis of the printer. The pieces were then removed from the printing platform and supports were detached. A 0.7 mm gauge pin was inserted into the through hole in the rotor holder and the funnel insert to clear out uncured resin while the threads on the top funnel and bottom cover were manually rinsed with isopropanol. All parts were rinsed with isopropanol in Formlab's Form Wash for 30 min. They were then allowed to dry completely, inspected for any remaining resin, and cured in Formlab's Form Cure for 60 min at  $60~^{\circ}$ C. The parts were then allowed to cool completely overnight before placing in the centrifuge, as newly cured parts are susceptible to deformation. Any remaining supports were detached with high-grit sandpaper. When packing rotors with larger microcrystals, the layer lines inside of the funnel should be carefully smoothed with sandpaper.

To pack a rotor, the end cap is first inserted into the designated rotor. The rotor holder is placed inside of the bottom cover and the rotor inserts into the central hole of the rotor holder, end cap down, until it touches the bottom cover base (Fig. 5). The top print is screwed into the assembly and inserted into an SW-60 Ti swinging bucket fitted for the Beckman Coulter ultracentrifuge. Approximately 1 mg of U— $^{13}\text{C},^{15}\text{N-A}\beta_{1-40}$  was micro pipetted into the funnel with spare supernatant to prevent the sample from drying, and the rotor was ultracentrifuged at 55 kHz for 4 h. After removing the packing tool assembly from the

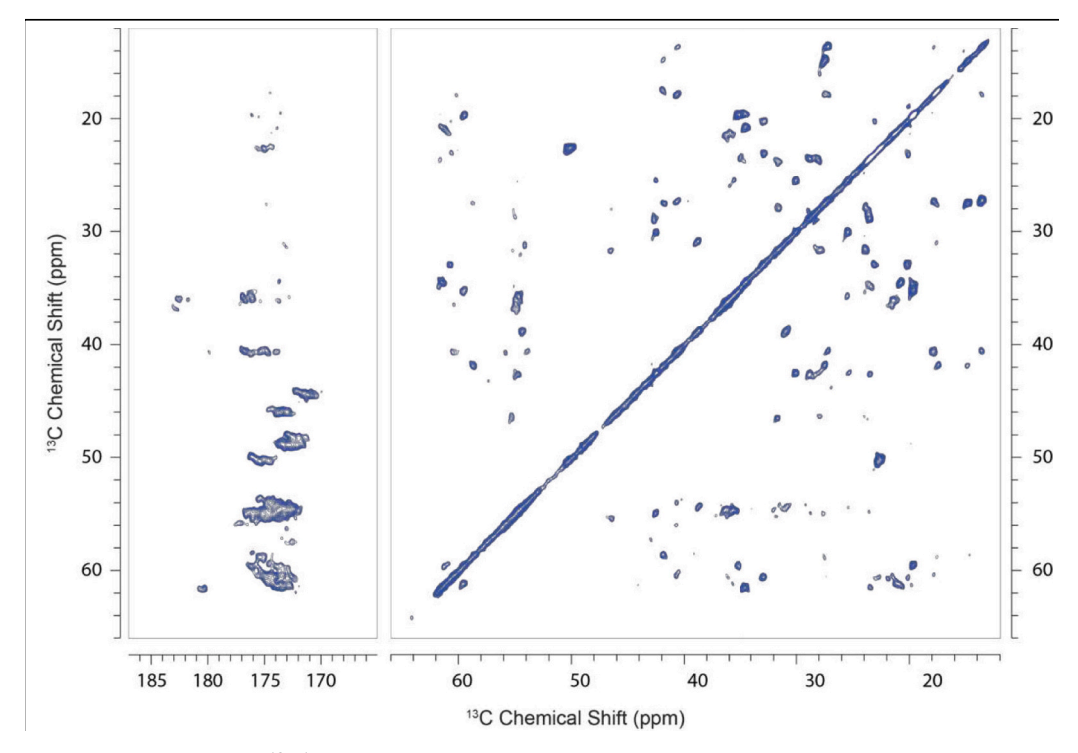


Fig. 8.  $^{13}$ C-detected hCC (RFDR) spectrum of U $^{-13}$ C,  $^{15}$ N A $\beta_{1-40}$  using a diamond rotor fabricated using centerless machining as described in the text and spinning at  $\omega_r/2\pi=100$  kHz at 277 K and in an 800 MHz spectrometer.

swinging bucket using a threaded removal tool, the supernatant and any excess sample were siphoned off from the funnel. The rotor was extracted and the end cap inspected for any damage. Weighing the rotor before and after filling suggested  $\sim 0.5$  mg of the sample was pelleted in the rotor. Packing was completed with commercially available Bruker 0.7 mm tools, where a small amount of excess sample was removed from the top of the rotor and the drive tip inserted. The exterior of the rotor was also cleaned to avoid supernatant contaminating the stator.

### 2.3. NMR experiments

All spectra were acquired at a static field of 18.8 T (800 MHz  $^{1}$ H) with a three channel (HCN) 0.7 mm Bruker MAS probe. The sample was spun at  $\omega_r/2\pi=100$  kHz using a Bruker MAS3 controller. The 90° pulse durations were 0.775  $\mu$ s, 2  $\mu$ s, and 3  $\mu$ s for  $^{1}$ H,  $^{13}$ C, and  $^{15}$ N, respectively.

## 2.3.1. 13C detected RFDR, hCC

CP from  $^1\text{H}$  to  $^{13}\text{C}$  was achieved with  $\tau_{mix}=2$  ms while the  $^1\text{H}$  RF amplitude was ramped tangentially ( $\pm 20$  %) around  $\omega_{1H}/2\pi=182$  kHz and  $^{13}\text{C}$  RF amplitude was held constant at  $\omega_{1C}/2\pi=74$  kHz. A low-power  $\omega_{1H}/2\pi=10$  kHz WALTZ decoupling field was used during  $t_1$  evolution and acquisition. RFDR mixing post  $t_1$  evolution was achieved using a train of 4  $\mu$ s  $\pi$  pulses for a mixing period of 1.6 ms.

# 2.3.2. <sup>1</sup>H-detected RFDR, hCCH

The pulse sequence for this experiment is as described by Golota, et al. [35], except that WALTZ decoupling was used in this work instead of SWTPPM decoupling. Forward CP from  $^1\mathrm{H}$  to  $^{13}\mathrm{C}$  was achieved with 2 ms of contact time while the  $^1\mathrm{H}$  RF amplitude was ramped tangentially (±20 %) around  $\omega_{1H}/2\pi=182$  kHz and  $^{13}\mathrm{C}$  RF amplitude was held constant at  $\omega_{1C}/2\pi=74$  kHz. Reverse  $^{13}\mathrm{C}$  to  $^1\mathrm{H}$  CP was achieved with 1.6 ms of contact time while the  $^1\mathrm{H}$  RF amplitude was ramped from  $\omega_{1H}/2\pi=154$  to 162 kHz and  $^{13}\mathrm{C}$  RF amplitude was held constant at  $\omega_{1C}/2\pi=74$  kHz. A low-power 10 kHz WALTZ decoupling was used during t1 and t2 evolutions. RFDR mixing post t1 evolution was achieved using a train of 4  $\mu\mathrm{s}$   $\pi$  pulses for a mixing period of 1.6 ms. Water

suppression was achieved using MISSISSIPPI pulse sequence with  $\omega_{1H}/2\pi=55$  kHz RF field for 200 ms.

### 3. Results and discussion

MAS NMR resolution is fundamentally limited by spinning frequency, which is constrained by the mechanical strength of the rotor material. Theoretical predictions suggest that to achieve solution-like linewidths and coherence lifetimes, MAS frequencies must exceed 300 kHz [36]. Traditional YSZ rotors, while widely used, are restricted in their ability to reach these frequencies due to material limitations. Commercially available 0.7 mm and 0.4 mm YSZ Bruker rotors are rated to spin at  $\omega_r/2\pi = 111$  kHz and 160 kHz, respectively. The group of Samoson has demonstrated spinning a 0.5 mm YSZ rotor up to  $\omega_r/2\pi =$ 170 kHz and more recently up to 200 kHz. At 200 kHz, the surface speed of a 0.5 mm rotor reaches approximately 90 % of the speed of sound in  $N_2$  at room temperature (~350 m/s), placing it in the mechanical failure region for ZrO<sub>2</sub> as discussed in Golota et al. [27,29] These limitations highlight the need for alternative rotor materials capable of supporting significantly higher spinning frequencies. HPHT diamond is a superior alternative, offering approximately three times the flexural strength of ZrO<sub>2</sub>, making it more suitable for higher spinning frequencies. In addition to its exceptional mechanical strength, HPHT diamond exhibits high thermal conductivity and excellent transparency to terahertz (THz) radiation, making it an ideal candidate for MAS DNP NMR experiments. As shown in our previous publications [27,29], theoretical models suggest that diamond rotors could support MAS frequencies 1.5-2.5 times higher than YSZ, significantly enhancing their utility in highresolution biomolecular and materials science applications.

Building upon our previous work on laser micromachining of diamond rotors, we have adopted a new machining approach that significantly improves concentricity, stability, and overall rotor performance. The first-generation diamond rotors, as described in our prior publication [27,29], were fabricated using rotary-assisted drilling, which, while effective, introduced significant concentricity errors. In contrast, our new fabrication protocol, detailed in the Methods section, utilizes a

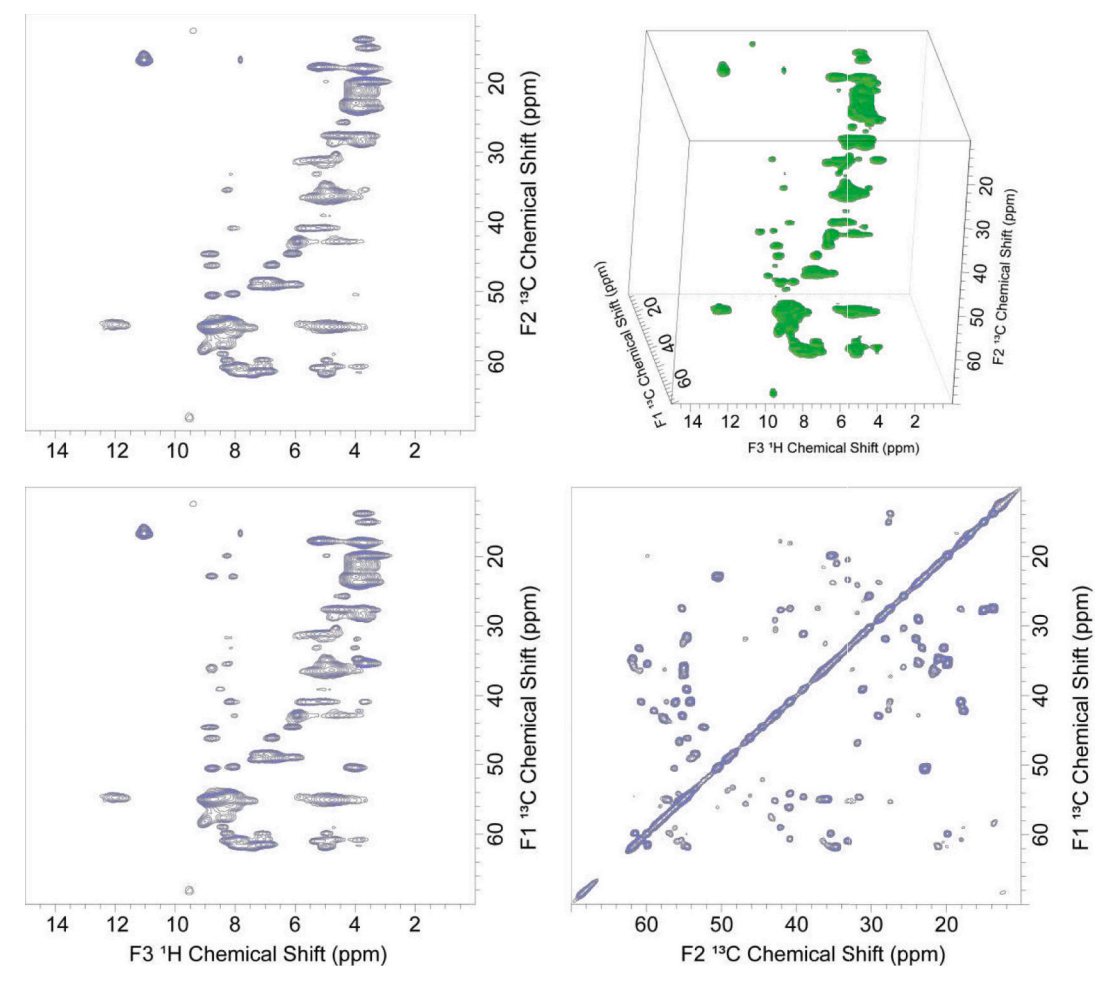


Fig. 9. 3D  $^{1}$ H-detected RFDR (hCCH) spectrum of U $^{-13}$ C,  $^{15}$ N-A $\beta_{1-40}$  spinning at 100 kHz at 277 K and in an 800 MHz spectrometer.

custom lathe with graphite air bearings for outer diameter (OD) machining and a centerless machining apparatus with free-spinning bearings, greatly enhancing precision. By securing the rotor between these free-spinning bearings, this method eliminates the need for external centering fixtures.

Six rotors were machined, as detailed in the Methods section, to match the specifications of the previous batch as reported in Ref. <sup>27</sup>, while accommodating Vespel drive tips and end caps, ensuring compatibility with Bruker Biospin (Billerica, MA, USA) zirconia rotor dimensions. To properly fit the longer stem of the drive tip, the rotors were oriented so that the end with the larger inner diameter (ID) housed the drive tip. Following this, the rotors were packed using the Bruker 0.7 mm rotor packing procedure with potassium bromide (Millipore-Sigma, Burlington, MA). Each rotor was inspected under a microscope for drive tip damage, end cap laser etchings, and any potential gaps between the diamond and Vespel to ensure optimal performance and durability.

Spin testing was conducted using dry  $\rm N_2$  spinning gas in the Bruker "MAS 3" Pneumatic Control Unit 3 (Bruker BioSpin, Billerica, MA, USA) and a 0.7 mm test stand system received from Bruker. All rotors were spun using Bruker's local automatic spinning mode, which applies preprogrammed ramp rates and optimized bearing and drive pressures. As with the previous batch, MAS frequency measurements were recorded at 1-s intervals using an oscilloscope, logged via a Python script, and analyzed in MATLAB (Mathworks, Natick, MA).

Rigorous testing involved spinning each rotor at  $\omega_r/2\pi=111$  kHz for one hour, along with at least two cycles of packing and repacking samples and standards to ensure stability and reusability in a 0.7 mm

Bruker probe. All six newly fabricated rotors were tested, with spin-up and stability profiles of four representative rotors are shown in Fig. 6. Standard deviations for spinning stability of rotors 1–4 were 3.29, 4.28, 3.83, and 3.72 Hz, respectively. Rotor 2 exhibited a brief drop in spinning frequency (~40 Hz), slightly increasing its standard deviation.

The spin-up profiles from 0 to 40 kHz MAS—where most rotor crashes typically occur—display a consistent near-linear dependence, indicating stable acceleration at moderate MAS frequencies.

Table 1 shows the drive pressures at the reported spinning frequencies for the rotors and demonstrates the remarkable similarities in drive pressures between diamond and zirconia rotors at several MAS frequencies, most differing by less than 50 or 100 millibar and no more than 200 millibar. The spinning behavior of diamond rotors is nearly identical to that of commercially available zirconia rotors, while the diamond rotors' robustness (during both handling and MAS spinning) and repackability allow for a highly improved user experience.

One of the rotors was repacked with  $\sim$ 0.5 mg of U—<sup>15</sup>N, <sup>13</sup>C-A $\beta_{1-40}$ , one of the primary proteins associated with Alzheimer's disease, using the rotor packing tool described above. The sample exemplifies a typical sample investigated in biomolecular NMR studies and Fig. 7 shows the 1D <sup>13</sup>C CPMAS spectra recorded at  $\omega_r/2\pi=100$  kHz in an 800 MHz spectrometer. The spectra obtained were free of any natural abundance <sup>13</sup>C background signal from the diamond rotor itself as the CPMAS sources the polarization from the <sup>1</sup>H spins. Besides, the <sup>13</sup>C spins in the diamond lattice relax on a timescale ( $\sim$ minutes) that is an order of magnitude longer than the <sup>13</sup>C spins in the protein sample, and therefore they do not contribute any background signal. The rotor spun stably for three weeks allowing execution of a number of different experiments.

For example, Fig. 8 shows a  $^{13}$ C-detected 2D  $^{13}$ C- $^{13}$ C RFDR spectrum, while Fig. 9 shows the  $^{13}$ C- $^{13}$ C RFDR projection of a 3D  $^{1}$ H-detected hCCH experiment. The experimental parameters are provided in the Methods section above. The experiments demonstrate the utility and compatibility of diamond rotors with commercially available MAS probes.

### 4. Conclusion

This work describes significant advances in the fabrication and performance of diamond MAS NMR rotors, addressing longstanding limitations in rotor materials and enabling ~100 kHz spinning frequencies that significantly enhance resolution, bringing MAS NMR linewidths closer to those of solution NMR. By employing centerless laser machining, we achieved substantial improvements in rotor concentricity and spinning stability, reducing eccentricity from  $6.5\ \mu m$ to 2 µm and increasing concentricity from 87 % to 96 %. These enhancements allow for stable spinning at 111 kHz, yielding performance comparable to commercial YSZ rotors while also offering the advantages of reusability and mechanical robustness. Furthermore, we introduced 3D-printed centrifuge tools for efficient and reproducible rotor packing, simplifying sample preparation for high-speed MAS NMR. The acquisition of high-resolution <sup>1</sup>H- and <sup>13</sup>C-detected MAS NMR spectra using our diamond rotors illustrate their utility for cutting-edge biomolecular and materials science applications and compatibility with commercially available MAS NMR probes.

Looking ahead, the intrinsic material advantages of diamond suggest that higher MAS frequencies (>150 kHz) should be achievable using helium gas as the driving fluid, paving the way for transformative improvements in MAS NMR resolution. To achieve this, future work will focus on optimizing stator components for reliable helium-driven spinning, ensuring that bearing and drive pressures are adapted for the higher kinematic viscosity of helium gas. Additionally, we plan to explore fabricating drive tips and end caps from diamond, further enhancing rotor stability and performance at extreme MAS frequencies beyond 150 kHz and at cryogenic temperatures (100K). Beyond improved spinning, diamond's high terahertz (THz) transmissibility presents an opportunity for improved DNP performance and this will be investigated.

# CRediT authorship contribution statement

Lauren Schaffer: Writing – original draft, Visualization, Validation, Investigation, Data curation. David Preiss: Writing - review & editing, Visualization, Validation, Methodology, Investigation, Formal analysis, Conceptualization. Ravi Shankar Palani: Writing - original draft, Validation, Methodology, Investigation, Formal analysis, Data curation. Nicholas Wiesner: Writing - review & editing, Methodology, Investigation, Formal analysis, Data curation. Jiaming Liu: Writing - review & editing, Methodology, Investigation, Data curation. Samuel Strymish: Visualization, Validation, Methodology, Investigation, Data curation. Salima Bahri: Validation, Methodology, Investigation, Data curation. Sara Linse: Writing - review & editing, Validation, Supervision, Methodology, Investigation, Funding acquisition, Conceptualization. Neil Gershenfeld: Writing - review & editing, Visualization, Validation, Supervision, Project administration, Funding acquisition, Conceptualization. Robert G. Griffin: Writing - review & editing, Writing original draft, Supervision, Conceptualization.

## Declaration of competing interest

The authors declare that they have no known competing financial interests or personal relationships that could have appeared to influence the work reported in this paper.

### Acknowledgement

The authors gratefully acknowledge the assistance of Sebastian Wegner and Armin Purea of Bruker BioSpin for support of the project including the supplied MAS3 and 0.7 mm test stand. We also acknowledge useful discussions and technical assistance from Natalie Golota, Zachary Fredin, Daniel Banks and Brian Michael. This research was supported by the National Institutes of General Medical Sciences (GM139055, GM132997 and AG058504).

### Appendix A. Supplementary data

Supplementary data to this article can be found online at https://doi.org/10.1016/j.jmr.2025.107909.

### Data availability

No data was used for the research described in the article.

### References

- V. Ladizhansky, R.S. Palani, M. Mardini, R.G. Griffin, Dipolar recoupling in rotating solids, Chem. Rev. 124 (2024) 12844–12917.
- [2] C.P. Jaroniec, C.E. MacPhee, V.S. Bajaj, M.T. McMahon, C.M. Dobson, R.G. Griffin, High-resolution molecular structure of a peptide in an amyloid fibril determined by magic angle spinning Nmr spectroscopy, Proc. Natl. Acad. Sci. USA 101 (2004) 711–716
- [3] A.T. Petkova, W.M. Yau, R. Tycko, Experimental constraints on quaternary structure in Alzheimer's Beta-amyloid fibrils, Biochemistry 45 (2006) 498–512.
- [4] C. Wasmer, A. Lange, H. Van Melckebeke, A.B. Siemer, R. Riek, B.H. Meier, Amyloid fibrils of the Het-S(218-289) prion form a Beta solenoid with a triangular hydrophobic Core, Science 319 (2008) 1523–1526.
- [5] A.W. Fitzpatrick, G.T. Debelouchina, M.J. Bayro, D.K. Clare, M.A. Caporini, V. S. Bajaj, C.P. Jaroniec, L. Wang, V. Ladizhansky, S.A. Muller, C.E. MacPhee, C. A. Waudby, H.R. Mott, A. De Simone, T.P. Knowles, H.R. Saibil, M. Vendruscolo, E. V. Orlova, R.G. Griffin, C.M. Dobson, Atomic structure and hierarchical assembly of a cross-Beta amyloid fibril, Proc. Natl. Acad. Sci. USA 110 (2013) 5468–5473.
- [6] A.K. Schuetz, T. Vagt, M. Huber, O.Y. Ovchinnikova, R. Cadalbert, J. Wall, P. Gntert, A. Bçckmann, R. Glockshuber, B.H. Meier, Atomic-resolution threedimensional structure of amyloid-B fibrils bearing the Osaka mutation, Angew. Chem. Int. Ed. 54 (2015) 331–335.
- [7] M.T. Colvin, R. Silvers, Q.Z. Ni, T.V. Can, I. Sergeyev, M. Rosay, K.J. Donovan, B. Michael, J. Wall, S. Linse, R.G. Griffin, Atomic resolution structure of monomorphic a Beta(42) amyloid fibrils, J. Am. Chem. Soc. 138 (2016) 9663–9674.
- [8] M.A. Walti, F. Ravotti, H. Arai, C.G. Glabe, J.S. Wall, A. Bockmann, P. Guntert, B. H. Meier, R. Riek, Atomic-resolution structure of a disease-relevant a Beta(1-42) amyloid fibril, Proc. Natl. Acad. Sci. USA 113 (2016) E4976–E4984.
- [9] M.D. Tuttle, G. Comellas, A.J. Nieuwkoop, D.J. Covell, D.A. Berthold, K. D. Kloepper, J.M. Courtney, J.K. Kim, A.M. Barclay, A. Kendall, W. Wan, G. Stubbs, C.D. Schwieters, V.M. Lee, J.M. George, C.M. Rienstra, Solid-state Nmr structure of a pathogenic fibril of full-length human alpha-synuclein, Nat. Struct. Mol. Biol. 23 (2016) 409–415.
- [10] R. Silvers, M.T. Colvin, K.K. Frederick, A.C. Jacavone, S. Lindquist, S. Linse, R. G. Griffin, Aggregation and fibril structure of Abetam01-42 and Abeta1-42, Biochemistry 56 (2017) 4850–4859.
- [11] U. Ghosh, K.R. Thurber, W.M. Yau, R. Tycko, Molecular structure of a prevalent amyloid-Beta fibril polymorph from Alzheimer's disease brain tissue, Proc. Natl. Acad. Sci. USA 118 (2021) 9.
- [12] V. Sridharan, T. George, D.W. Conroy, Z. Shaffer, W.K. Surewicz, C.P. Jaroniec, Copper binding alters the Core structure of amyloid fibrils formed by Y145stop human prion protein, Phys. Chem. Chem. Phys. 26 (2024) 26489–26496.
- [13] V.S. Bajaj, M.L. Mak-Jurkauskas, M. Belenky, J. Herzfeld, R.G. Griffin, Functional and shunt states of bacteriorhodopsin resolved by 250 Ghz dynamic nuclear polarization-enhanced solid-state Nmr, Proc. Natl. Acad. Sci. USA 106 (2009) 9244–9249.
- [14] F. Hu, W. Luo, M. Hong, Mechanisms of proton conduction and gating in influenza M2 proton channels from solid-state Nmr, Science 330 (2010) 505–508.
- [15] S.D. Cady, K. Schmidt-Rohr, J. Wang, C.S. Soto, W.F. DeGrado, M. Hong, Structure of the amantadine binding site of influenza M2 proton channels in lipid bilayers, Nature 463 (2010) 689–692.
- [16] Q.Z. Ni, T.V. Can, E. Daviso, M. Belenky, R.G. Griffin, J. Herzfeld, Primary transfer step in the light-driven ion pump bacteriorhodopsin: an irreversible U-turn revealed by dynamic nuclear polarization-enhanced magic angle spinning Nmr, J. Am. Chem. Soc. 140 (2018) 4085–4091.
- [17] A.C. Sivertsen, M.J. Bayro, M. Belenky, R.G. Griffin, J. Herzfeld, Solid-state Nmr characterization of gas vesicle structure, Biophys. J. 99 (2010) 1932–1939.
- [18] L. Bhai, J.K. Thomas, D.W. Conroy, Y. Xu, H.M. Al-Hashimi, C.P. Jaroniec, Hydrogen bonding in duplex DNA probed by Dnp enhanced solid-state Nmr N-H bond length measurements, Front. Mol. Biosci. 10 (2023) 1286172.

- [19] D.W. Conroy, Y. Xu, H. Shi, N. Gonzalez Salguero, R.N. Purusottam, M.D. Shannon, H.M. Al-Hashimi, C.P. Jaroniec, Probing Watson-crick and Hoogsteen Base pairing in duplex DNA using dynamic nuclear polarization solid-state Nmr spectroscopy, Proc. Natl. Acad. Sci. USA 119 (2022) e2200681119.
- [20] C.P. Jaroniec, Structural and dynamic studies of chromatin by solid-state Nmr spectroscopy, Curr. Opin. Struct. Biol. 89 (2024) 102921.
- [21] R. Bhattacharyya, B. Key, H. Chen, A.S. Best, A.F. Hollenkamp, C.P. Grey, In situ Nmr observation of the formation of metallic Lithium microstructures in Lithium batteries, Nat. Mater. 9 (2010) 504–510.
- [22] P. Berruyer, L. Emsley, A. Lesage, Dnp in materials science: touching the surface, Emagres 7 (2018) 93–104.
- [23] M. Schledorn, A.A. Malär, A. Torosyan, S. Penzel, D. Klose, A. Oss, M.L. Org, S. Wang, L. Lecoq, R. Cadalbert, A. Samoson, A. Böckmann, B.H. Meier, Protein Nmr spectroscopy at 150 Khz magic-angle spinning continues to improve resolution and mass sensitivity, Chembiochem 21 (2020) 2540–2548.
- [24] S. Penzel, A. Oss, M.L. Org, A. Samoson, A. Bockmann, M. Ernst, B.H. Meier, Spinning faster: protein Nmr at mas frequencies up to 126khz, J. Biomol. NMR 73 (2019) 19–29.
- [25] Samoson, A.; Tuherm, T.; Past, J.; Reinhold, A.; Anup~old, T.; Heinmaa, I., New horizons for magic-angle spinning Nmr top. Curr. Chem. 2005, 246, 15–31.
- [26] V. Agarwal, S. Penzel, K. Szekely, R. Cadalbert, E. Testori, A. Oss, J. Past, A. Samoson, M. Ernst, A. Bockmann, B.H. Meier, De Novo 3d structure determination from sub-milligram protein samples by solid-state 100 Khz mas Nmr spectroscopy, Ange. Chem.-Int. Ed. 53 (2014) 12253–12256.
- [27] N.C. Golota, Z.P. Fredin, D.P. Banks, D. Preiss, S.B.P. Patil, W.K. Langford, C. L. Blackburn, E. Strand, B. Michael, B. Dastrup, K.A. Nelson, N. Gershenfeld, R. Griffin, Diamond rotors, J. Magn. Reson. 352 (2023) 107475.

- [29] N.C. Golota, D. Preiss, Z.P. Fredin, P. Patil, D.P. Banks, S. Bahri, R.G. Griffin, N. Gershenfeld, High aspect ratio diamond nanosecond laser machining, Appl. Phys. a-Mater. Sci. & Processing (2023) 129.
- [30] R.S. Palani, M. Mardini, Y.F. Quan, Y.F. Ouyang, A. Mishra, R.G. Griffin, Dynamic nuclear polarization with P1 Centers in diamond, J. Phys. Chem. Lett. 15 (2024) 11504–11509.
- [31] R.H. Telling, C.J. Pickard, M.C. Payne, J.E. Field, Theoretical strength and cleavage of diamond, Phys. Rev. Lett. 84 (2000) 5160–5163.
- [32] T.M. Osborn Popp, B.T. Matchett, R.G. Green, I. Chhabra, S. Mumudi, A. D. Bernstein, J.R. Perodeau, A.J. Nieuwkoop, 3d-printable centrifugal devices for biomolecular solid state Nmr rotors, J. Magn. Reson. 354 (2023) 107524.
- [33] M.A. Olson, R. Han, T. Ravula, C.G. Borcik, S. Wang, P.A. Viera, C.M. Rienstra, A complete 3d-printed tool kit for solid-state Nmr sample and rotor handling, J. Magn. Reson. 366 (2024) 107748.
- [34] G.S. Hisao, M.A. Harland, R.A. Brown, D.A. Berthold, T.E. Wilson, C.M. Rienstra, An efficient method and device for transfer of semisolid materials into solid-state Nmr spectroscopy rotors, J. Magn. Reson. 265 (2016) 172–176.
- [35] N.C. Golota, B. Michael, E.P. Saliba, S. Linse, R.G. Griffin, Structural Characterization of E22g Aβ
  Sub>1-42</Sub> Fibrils <I>Via </I><Sup>1
  Sup>H Detected Mas Nmr, Phys. Chem. Chem. Phys. 26 (2024) 14664.
- [36] K. Xue, R. Sarkar, C. Motz, S. Asami, V. Decker, S. Wegner, Z. Tosner, B. Reif, Magic-angle spinning frequencies beyond 300 Khz are necessary to yield maximum sensitivity in selectively methyl protonated protein samples in solid-state Nmr, J. Phys. Chem. C 122 (2018) 16437–16442.